1996ApJ...464..724K

THE ASTROPHYSICAL JOURNAL, 464:724–737, 1996 June 20

NUMERICAL SIMULATION OF BENT JETS: PROPAGATION INTO AN OBLIQUE MAGNETIC FIELD

SHINJI KOIDE AND JUN-ICHI SAKAI
Laboratory of Plasma Astrophysics and Fusion Science, Faculty of Engineering, Toyama University, Gofuku, Toyama 930, Japan
AND
KEN-ICHI NISHIKAWA[1] AND ROBERT L. MUTEL
Department of Physics and Astronomy, University of Iowa, Iowa City, IA 52242
Received 1995 June 16; accepted 1996 January 8

ABSTRACT

We have investigated the propagation of a fluid jet through an oblique uniform magnetic field using a three-dimensional ideal magnetohydrodynamic model. The numerical experiments show that the jet is bent by the oblique magnetic field. We found that the bending scale depends on the jet velocity and jet–magnetic field angle. The high magnetic Mach number jet goes straight compared with the slow jet. The magnetic field with the angle between the jet and magnetic field 45° bends the jet most quickly. The plasma and the perpendicular component of the magnetic field are compressed at the head of the jet. We found also that the oblique magnetic field decelerates the speed of the jet head. These numerical results are explained by a simple analytical model. We apply these results to explain the peculiarities of BL Lacertae objects among active galactic nuclei (AGNs) from a unified point of view: interaction between the jet from AGNs and the extragalactic magnetic field.

Subject headings: galaxies: jets — methods: numerical — MHD

1. INTRODUCTION

Observational studies of jets in extragalactic radio sources show that the jets are often bent through large apparent angles (e.g., Fejes, Porcas, & Akujar 1992; Hummel et al. 1992; Conway & Davis 1994). The bending could result from a variety of causes, including helical trajectories due to Kelvin-Helmholtz instabilities (e.g., Hardee 1987; Hardee & Clarke 1992; Hardee et al. 1992; Conway & Murphy 1993), a precessing of a binary engine (Begelman, Blandford, & Rees 1980), or deflection of the jet in a dense ambient medium (e.g., Ludke 1994). In this paper, we investigate the bending and other aspects of jets interacting with an uniform ambient magnetic field oriented obliquely to the jet axis.

Several hydrodynamical simulations have been used for study of Kelvin-Helmholtz instability for bending jets (e.g., Zhao et al. 1992; Hardee, Michael, & Clarke 1994). Hardee et al. (1994) performed simulations with an unstable supersonic (two-dimensional) slab-symmetric jet. The instabilities within the jet are characterized by growing internal body waves and their coupled surface waves that are also predicted in linear perturbation theory. They demonstrated that sound waves can be excited by imposing an arbitrary disturbance. These waves eventually disrupt the jet at a certain length. The disruption length is related to the jet Mach number and the perturbation strength. However, since most astrophysical jets are likely to be affected by ambient magnetic fields, we believe that it is very important to use a magnetohydrodynamic (MHD) code instead of a hydrodynamic code. An ambient magnetic field can affect the jet propagation substantially as well as the observed synchrotron emission. Furthermore, it is very important to use a three-dimensional MHD code rather than a two-dimensional code (which have been used in previous simulations) to simulate jet propagation in a magnetic field.

We have performed numerical, three-dimensional ideal MHD simulations of a nonrelativistic jet injected into an oblique uniform magnetic field. On the first stage, the jet goes across the oblique magnetic field pushing aside the magnetic line of force. The jet is eventually bent by the magnetic field into the direction of the initial magnetic field. The bending scale or scattering angle of the jet depends on the jet Mach number and jet–magnetic field angle. A small Mach number jet is bent easily compared with a fast jet. The magnetic field with the jet–magnetic field angle 45° bends the jet most quickly. The numerical experiments confirm that the perpendicular component of the magnetic field is compressed at the jet head as well as plasma density and pressure. We also found the deceleration effect of the jet head speed by the oblique magnetic field. These numerical results are explained by a simple analytical model. We are aware that our nonrelativistic MHD simulations cannot be applied to explain observations with BL Lac objects directly. Furthermore, BL Lac objects consist of electron-positron plasmas; therefore, an electromagnetic, relativistic particle code (Zhao et al. 1994) would be necessary to include kinetic effects which are essential in electron-positron plasmas. However, the main features of our simulations would apply in observations with BL Lac objects.

Recently, three kinds of peculiarities of BL Lacertae in parsec scale compared to quasars are found by using VLBI (Very Long Baseline Interferometer) observations. First, in the parsec scale, the magnetic field is perpendicular to the BL Lacertae object elongation while parallel to the nuclear jets in quasars (Gabuzda 1992). Second, the flow speeds of BL Lacertae objects are systematically less than those of quasars (Gabuzda et al. 1989a, 1994). The third peculiarity is a statistical remark; that is, for almost all BL Lacertae objects, one-sided jet structures at parsec and kiloparsec scales are strongly misaligned, while for some of quasars and extragalactic jets they are more nearly aligned (e.g., Mutel 1989; Appl, Sol, & Vicente 1995; Sol, Appl, & Vicente 1995). Sol (1992a) and Sol & Vicente (1994, 1995)

---

[1] Present address: Department of Space Physics and Astronomy, Rice University, Houston, TX 77251.

proposed the model of the jet injected into the oblique magnetic field to explain parts of these peculiarities. They considered the oblique coherent magnetic field tied with the accretion disk whose rotation axis is different from the jet axis. But the scale of the accretion disk is much smaller than 1 pc, which is order of the VLBI resolution, so it is improbable that such a magnetic field held by the accretion disk has any influence on the parsec-scale structure of BL Lacertae objects. Considering that observed polarization variation is explained by the *random walks* generated through evolution of the turbulent magnetic field (Jones et al. 1985), the model of the jet injected into the turbulent ambient magnetic field is more plausible. These four peculiarities of BL Lacertae objects among AGNs may be explained by an unified model: the extragalactic magnetic field of 1″ scale around BL Lacertae objects is turbulent, while that around quasars is coherent.

In the next section, we explain the numerical model. Section 3 presents the numerical results. In § 4, a simple analytical model is presented and compared with the numerical model. A summary and discussion are given in § 5.

2. NUMERICAL MODEL

We used ZEUS-3D, a nonrelativistic ideal magnetohydrodynamic (MHD) code which solves the equations of astrophysical fluid dynamics (AFD) on a three-dimensional Eulerian grid (Stone & Norman 1992a, b). The AFD equations can be divided into three parts: hydrodynamics (HD), magnetohydrodynamics (MHD), and radiative hydrodynamics (RHD). We have used the MHD equations only, namely,

$$\frac{\partial \rho}{\partial t} + \nabla \cdot (\rho \boldsymbol{V}) = 0 \,, \qquad (1)$$

$$\frac{\partial \rho \boldsymbol{V}}{\partial t} + \nabla \cdot (\rho \boldsymbol{V} \boldsymbol{V}) = -\nabla p + \boldsymbol{J} \times \boldsymbol{B} \,, \qquad (2)$$

$$\frac{\partial e}{\partial t} + \nabla \cdot (e \boldsymbol{V}) = -p \nabla \cdot \boldsymbol{V} \,, \qquad (3)$$

$$\frac{\partial \boldsymbol{B}}{\partial t} = \nabla \times (\boldsymbol{V} \times \boldsymbol{B}) \,, \qquad (4)$$

$$\boldsymbol{J} = \nabla \times \boldsymbol{B} \,, \qquad (5)$$

where ρ, $\boldsymbol{V}$, p, $\boldsymbol{B}$, $\boldsymbol{J}$, and e are matter density, velocity, thermal pressure, magnetic field, current density, and internal energy density (per unit volume) $e \equiv p/(\gamma - 1)$, where $\gamma(=5/3)$ is the adiabatic constant, respectively. We normalize the magnetic permeability μ to unity.

We used finite differencing on an Eulerian mesh using Cartesian coordinates. The equations are solved fully explicitly in time, and therefore numerical stability is subject to the Courant condition. The code solves the integral form of the MHD equations by dividing the fluid field into numerous small cells called control volumes and considers the change of these quantities within each control volume from one time step to the next. Each control volume has a cell center, six cell faces, and eight cell corners. Scalars and tensors of even rank (i.e., ρ, e, and p) are put at the cell center, and vectors (i.e., $\boldsymbol{V}$, $\boldsymbol{B}$) are at the centers of each cell face. This is a kind of "staggered mesh." Shocks are smeared over several zones using a von Neumann–Richtmyer artificial viscosity. We used the upstream algorithm for solving the hyperbolic equations (see Stone & Norman 1992a,b for a detailed discussion of the numerical algorithms incorporated in ZEUS-3D).

2.1. *Initial Condition*

The jet is initially injected into an ambient plasma with an oblique uniform magnetic field. The simulation was constrained to a box with coordinates $0 \leq x \leq 4$, $-2 \leq y \leq 2$, $-2 \leq z \leq 2$ (arbitrary units) and spatial resolution 0.05 in each dimension ($80 \times 80 \times 80$ cells). The jet is injected along the x-axis at the $x = 0$ surface. A schematic picture is shown in Figure 1. The initial parameters inside the calculation box are as follows:

$$\rho = \rho_a \,, \qquad (6)$$

$$\boldsymbol{V} = 0 \,, \qquad (7)$$

$$e = e_a \,, \qquad (8)$$

$$\boldsymbol{B} = (B_{1a}, B_{2a}, 0) = (B_a \cos\theta, B_a \sin\theta, 0), \qquad (9)$$

where we set the normalized ambient mass density $\rho_a = 2$, energy density $e_a = 1$, and the magnetic field $B_a = 1.41$. In this case, the sound speed is $v_s \equiv [\gamma(\gamma - 1)e/\rho]^{1/2} = 0.745$, Alfvén velocity is $v_{\rm A} \equiv (B^2/\rho)^{1/2} = 1.0$, and the speed of the fast wave is $v_f \equiv (v_{\rm A}^2 + v_s)^{1/2} = 1.25$. Equipartition is assumed between the thermal and magnetic field energies. Simulations were run with initial jet-field angles of $\theta = 15°$ and $\theta = 45°$.

2.2. *Boundary Conditions*

We used the outflow boundary or radiative condition for the surfaces of the simulation box except for the orifice of the jet at the $x = 0$ surface. We used the inflow boundary condition only for the orifice. The boundary condition of

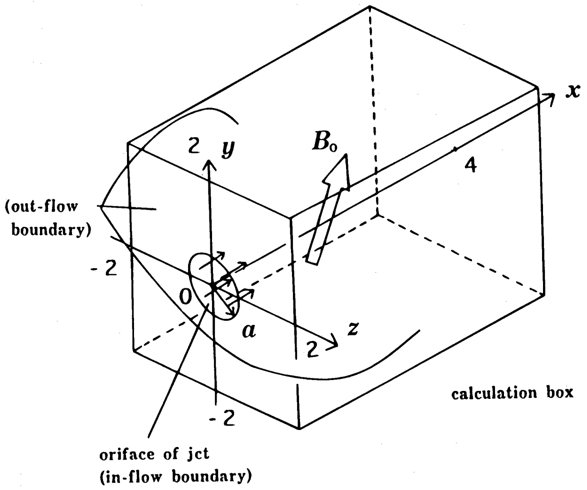

FIG. 1.—Schematic picture of the initial and boundary conditions of jet injected oblique to the magnetic field. The jet is injected along the x-direction from the orifice placed at the origin of the coordinates. Initially density, pressure, and magnetic field are uniform, and the velocity is zero. The radius of the orifice is a (=0.2). The boundary condition is outflow boundary except for the orifice, and inflow boundary for the orifice. Note that there is no perpendicular magnetic field inside the jet.

the orifice $r \equiv (y^2 + z^2)^{1/2} \leq a + d, x = 0$ is given by

$$\rho = \rho_0 = \rho_a \,, \tag{10}$$

$$V = (f(r, v_0, a, d), 0, 0) \,, \tag{11}$$

$$p = p_a \,, \tag{12}$$

$$B = (B_{1a}, f(r, 0, B_{2a}, a, d), 0) \,, \tag{13}$$

where $f(x, f_1, f_2, a, d) = (f_1 + f_2)/2 + (f_2 - f_1) \tanh [(x - a)/d)]/2$ is a smoothed step function. Here a corresponds to the radius of the jet, and d is a smoothing factor which gives smooth edges for the jet velocity and magnetic field at the boundary between the jet and ambient plasma. On the surface $x = 0$ and $r > a + d$, we use the ouflow boundary to avoid the numerical instabilities near the $x = 0$ surface. Here we set $a = 0.2$ and $d = 0.05$. We perform $v_0 = 2v_A$, $2.5v_A$, $3v_A$, $4v_A$, and $7v_A$ cases. Due to this boundary condition, the jet does not contain the perpendicular magnetic field (M. L. Norman, private communication).

3. NUMERICAL RESULTS

3.1. *Morphological Structure of Jet Oblique to an Ambient Magnetic Field*

We present the numerical experimental results of the jet injected into the magnetic field. We have performed five large-angle ($\theta = 45°$) cases (A: $v_0 = 2v_A$; B: $v_0 = 2.5v_A$; C: $v_0 = 3v_A$; D: $v_0 = 4v_A$; E: $v_0 = 7v_A$) and two small-angle ($\theta = 15°$) cases (F: $v_0 = 4v_A$; G: $v_0 = 7v_A$).

3.1.1. *High-Angle Cases* ($\theta = 45°$)

First, in order to investigate the dependence of the initial velocity v_0 of the jets injected with $\theta = 45°$, four cases, A ($v_0 = 2v_A$), B ($v_0 = 2.5v_A$), D ($v_0 = 4v_A$), and E ($v_0 = 7v_A$), are compared. Figure 2 shows the velocity (Figs. 2*a*, 2*c*, 2*e*, 2*g*) and the magnetic field (Figs. 2*b*, 2*d*, 2*f*, 2*h*) on the *xy*-plane (at $z = 0$). The jet was injected toward the *x*-direction from the orifice at $x = 0$. The jet orifice is centered at the origin of the coordinates and has a radius $a = 0.2$. In the velocity plot of case A at $t = 1.87\tau_A$ (Fig. 2*a*), the jet moves along the *x*-axis near the orifice but is deflected toward the direction of the initial magnetic field as it propagates along. Here the Alfvén transit time τ_A is defined by the traveling time of the Alfvén wave with the distance 1 in the ambient plasma. The jet expands near the head of the jet. The ambient magnetic field is distorted and compressed by the jet, as shown in Figure 2*b*. As the jet speed is slightly increased (case B, $v_0 = 2.5v_A$), the same plots at $z = 0$ are shown in Figures 2*c*–2*d* at $t = 1.64\tau_A$. It is clear that the jet goes straight through the oblique magnetic field more deeply than in case A ($x \approx 2.0$, $y \approx 0.2$). The velocity plot (Fig. 2*c*) shows two separate streamers. One of them goes straight along the *x*-axis, and the other moves along the $\theta = 45°$ lines. The latter is caused by the magnetic field distorted by the jet as a *slingshot*. The jet velocity was increased again in case D ($v_0 = 4v_A$). The cross sections of the jet at $t = 1.42\tau_A$ are shown in Figures 2*e*–2*f*. The jet goes almost straight through the oblique magnetic field as shown in the velocity plot (Fig. 2*e*). The slight flow dragged by the distorted magnetic field is found at the upper boundary of the straight jet ($x \approx 1.5$, $y \approx 0.8$) (Figs. 2*e*–2*f*), the same as in case B. The jet expands near the orifice and is pinched near the jet head. For the highest jet velocity in our simulation (case E, with $v_0 = 7v_A$), the cross sections of the jet are shown in Figures 2*g*–2*h* at $t = 1.24\tau_A$. The velocity plot (Fig. 2*g*) shows that the jet goes straight through the oblique magnetic field. The slight expansion of the jet near the orifice is found. The jet is also pinched near the jet head. The magnetic field plot (Fig. 2*h*)·indicates the strongly distorted (reversed) magnetic field lines above the jet. The distorted field lines accelerate the ambient plasma (Fig. 2*g*) as in the other cases, but the flow is slight. Obviously, the jet with the high velocity propagates further and moves straight.

Due to the different propagation of the jets depending on their speed, the mass density (Figs. 2*a*, 2*c*, 2*e*, 2*g*) and pressure (Fig. 2*b*, 2*d*, 2*f*, 2*h*) also show the differences as shown in Figure 3 at the same time for each case in Figure 2. In case A, the density and pressure are also compressed at the jet head, $x \approx 1.5$, $y \approx 1.2$ (Figs. 3*a*–3*b*). We see the low-density and low-pressure region at the base of the jet. This is because plasma is swept by the magnetic field dragged by the jet ($x \approx 0.2$, $y \approx 0.3$). This is a characteristic of jets injected to an oblique magnetic field. There is a slight bow shock at $x = 2$. For case B, the density and pressure have two peaks at $x \approx 1.2$, $y \approx 1.2$ and $x \approx 2.0$, $y \approx 0.2$ (Figs. 3*c*–3*d*). The former corresponds to the head of the streamer caused by the distorted magnetic field. The latter corresponds to the jet head. We also see the low-density and low-pressure region at the base of the jet, the same as in case A. An asymmetric slight bow shock is also found in the density and pressure plots (Figs. 3*c*–3*d*). For case D, the highest density region is located at the jet head only (Fig. 3*e*). The highest density region is merged into the bow shock. For case E, a high-density region is found only at the jet head (Fig. 3*g*). The pressure at the jet head is much higher than that of the bow shock compared with the other cases (Fig. 3*h*). The bow shock is located at the magnetic shear, as expected, and it is almost symmetric around the jet axis.

3.1.2. *Low-Angle Cases* ($\theta = 15°$)

We have also investigated cases with the initial jet–magnetic field angle $\theta = 15°$. Figure 4 shows the velocity (Figs. 4*a*, 4*c*) and magnetic field (Figs. 4*b*, 4*d*) on the *x*-*y* plane at $z = 0$ of cases F ($v_0 = 4v_A$) at $t = 1.74\tau_A$ (Figs. 4*a*–4*b*) and G ($v_0 = 7v_A$) at $t = 1.0\tau_A$ (Figs. 4*c*–4*d*). The density and pressure plots for the same cases at the same time are plotted in Figure 5. The jet (case F) goes straight (Fig. 4*a*) without the expansion near the orifice found in case D ($v_0 = 4v_A$, $\theta = 45°$) (see Fig. 2*e*). The magnetic field plot indicates the very strongly distorted magnetic field lines which are expected to accelerate the ambient plasma around the jet very rapidly (Figs. 4*a*–4*b*). The accelerated plasma forms a high-density region, as shown in the density plot (Fig. 5*a*). The high-density region is separated from the bow shock. On the other hand, the high-pressure region is located at the jet head only (Fig. 5*b*).

Case G ($v_0 = 7v_A$) is shown in Figures 4*c*–4*d* and 5*c*–5*d* at $t = 1.0\tau_A$. The jet also goes straight without the expansion near the orifice, in comparison with case E ($v_0 = 7v_A$, $\theta = 45°$) (see Figs. 2*g*–2*h* and 3*g*–3*h*). The magnetic field plot indicates the very strong distorted field lines (Fig. 4*d*). The slightly high density region between the jet and the upstream bow shock is due to acceleration by the distorted magnetic field, as shown in Figure 5*c*. The bow shock is clearly symmetric. In this case, both high-density and high pressure are located at the jet head (Figs. 5*c*–5*d*). These simulations confirm the intuitive results that the jets go more nearly straight with smaller bending angle ($\theta = 15°$)

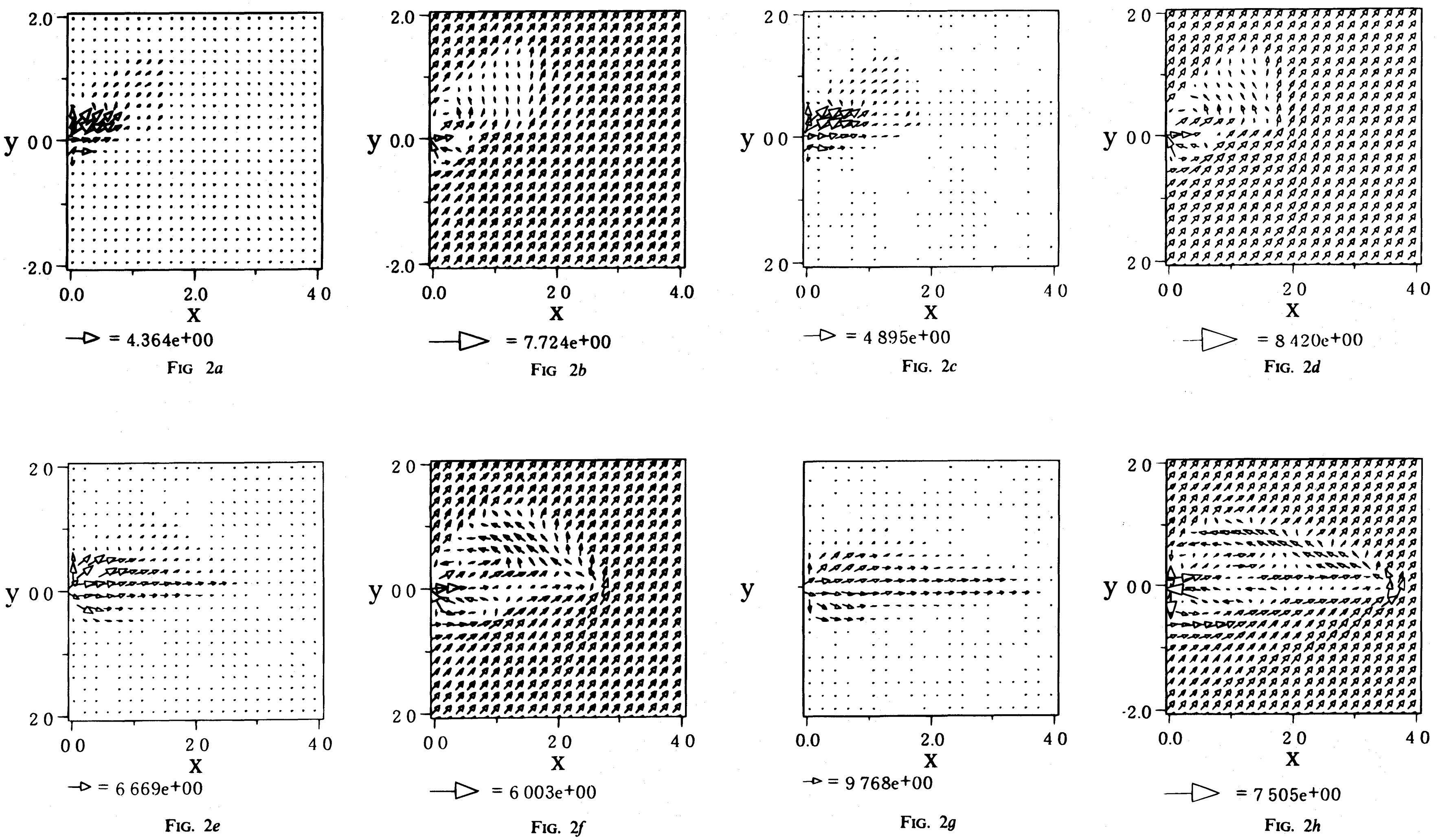

FIG 2a

FIG 2b

FIG. 2c

FIG. 2d

FIG. 2e

FIG. 2f

FIG. 2g

FIG. 2h

FIG. 2.—Comparison of velocity (*a*, *c*, *e*, *g*) and the magnetic field (*b*, *d*, *f*, *h*) for cases A, B, D, and E. (*a*, *b*) Case A ($v_0 = 2v_A$) at $t = 1.87\tau_A$. (*c*, *d*) Case B ($v_0 = 2.5v_A$) at $t = 1.64\tau_A$. (*e*, *f*) Case D ($v_0 = 4v_A$) at $t = 1.42\tau_A$. (*g*, *h*) Case E ($v_0 = 7v_A$) at $t = 1.24\tau_A$.

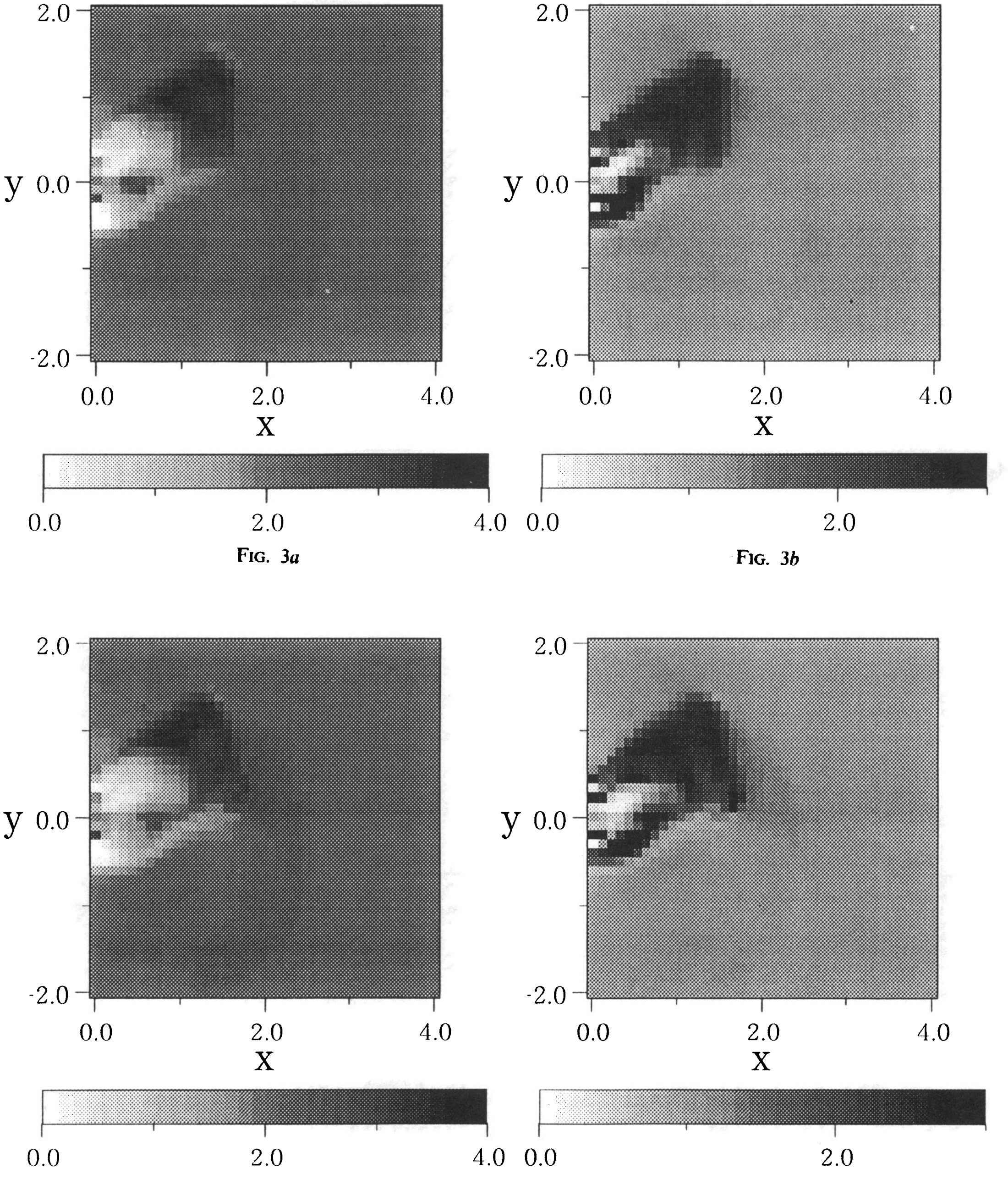

FIG. 3a

FIG. 3b

FIG. 3c

FIG. 3d

FIG. 3.—Comparison of density (*a, c, e, g*) and pressure (*b, d, f, h*) profiles for cases A, B, D, and E. (*a, b*) Case A ($v_0 = 2v_A$) at $t = 1.87\tau_A$. (*c, d*) Case B ($v_0 = 2.5v_A$) at $t = 1.64\tau_A$. (*e, f*) Case D ($v_0 = 4v_A$) at $t = 1.42\tau_A$. (*g, h*) Case E ($v_0 = 7v_A$) at $t = 1.24\tau_A$.

between the jet velocity and the ambient magnetic field than large-angle cases ($\theta = 45°$).

3.1.3. *Three-dimensional Structure of the Jet*

Figure 6 shows the three-dimensional structure of the jet and magnetic field for case E ($\theta = 45°$, $v_0 = 7v_A$). The gray object is the velocity isosurface $v_x = 1.27v_A$, which indicates the shape of the jet. The orifice of the jet is the light gray circular object on the *y*-*z* plane. Note the expansion near the orifice and the pinching near the jet head. The magnetic field lines are distorted to let the jet pass through. This three-dimensional effect is important for propagation across the oblique magnetic field. Without this three-dimensional effect, the magnetic pressure at the jet head increases drastically, and the jet cannot propagate through the oblique magnetic field.

3.2. *Analysis of Numerical Experiment*

We have analyzed the bending, compressibility, and deceleration of the jet head by the oblique magnetic field with numerical experiments. First we discuss the bending scale and scattering angle of the jet by the oblique magnetic field. Figure 7 shows the density (Figs. 7*a*, 7*c*) and velocity (Figs. 7*b*, 7*d*) of case A when $t = 1.00\tau_A$ (Figs. 7*a*–7*b*) and $t = 1.87\tau_A$ (Figs. 7*c*–7*d*). The velocity of the jet along the *x*-axis near $y = 0$ at $t = 1.87\tau_A$ is smaller than that of $t = 1.00\tau_A$. However, the velocity along the ambient magnetic field ($\theta = 45°$) increases, which shows a bending of the jet. We define the bending scale of the jet as the total length traveled by the jet along the *y*-axis as its direction changes from the *y*-direction to the direction of the ambient magnetic field. For case A, the bending scale is 4.55*a*. The

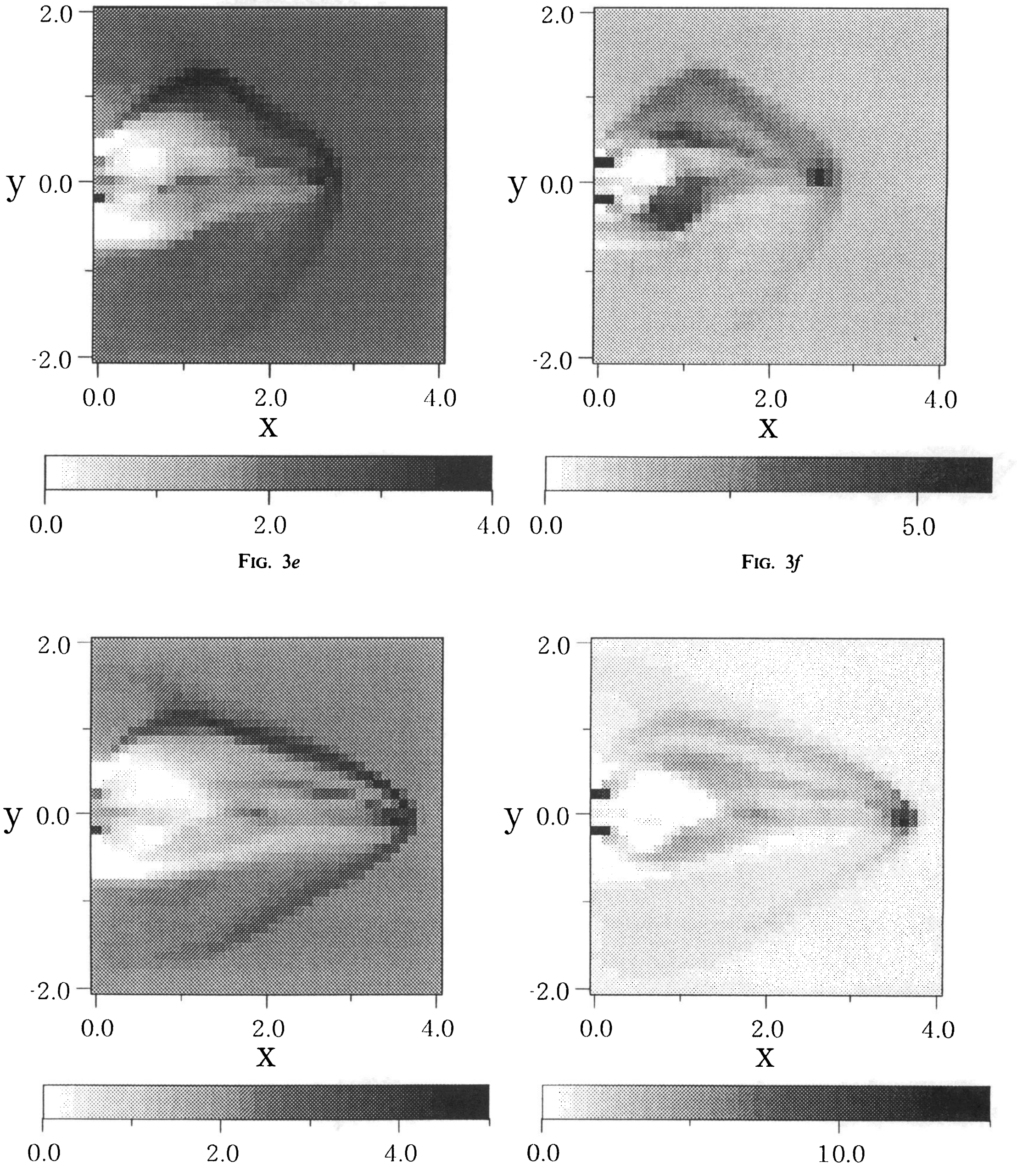

FIG. 3e

FIG. 3f

FIG. 3g

FIG. 3h

FIG. 3—*Continued*

bending scales of all cases are summarized in Table 1 (col. [4]). Unfortunately, the bending of the jet in cases D, E, F, and G is not observed because the jet bending is too small to detect.

To determine the scattering angle $\Delta\theta \equiv \tan^{-1}(v_y/y_x)$ of the jet by the oblique magnetic field, the jet head is identified by the large velocity and high density. From Figure 7 (case A), we calculate the average velocity $\bar{v}_x = 0.702v_A$, $\bar{v}_y = 0.636v_A$ between $t = 1.00\tau_A$ and $t = 1.87\tau_A$ to evaluate the velocity of the jet head (Table 2, cols. [2] and [3], first row) (L is the traveling distance). We can also calculate the tangent of the scattering angle of the jet by these velocities (Table 2, col. [4]). The velocity is calculated by this method for the jet head for each case, and values are summarized in Table 2 (cols. [2] and [3]). The tangent of the scattering angle is also calculated for all other cases (Table 2, col. [4]). The scattering angle of the cases E, F, and G is too small to detect in this numerical experiment.

Now we analyze the compression of the plasma and magnetic field at the jet head. Figure 8 shows (*a*) the mass density, (*b*) the y-component of the magnetic field, and (*c*) the internal energy (pressure) of case D at $y = 0.2$, $z = 0$ along the x-axis, which is almost along the jet and contains the jet head at $t = 1.42\tau_A$. The maxima of density and pressure are located at $x \approx 2.60$ (see Figs. 8*a*, 8*c*). The maximum of B_y is located at $x \approx 2.75$ (Fig. 8*b*). The density and pressure maxima correspond to the working surface of the jet. The later maximum is caused by the ambient magnetic field compression, therefore it is located in front of the working surface. The mass density at $x \leq 1$ is smaller than the initial ambient density $\rho_a = 2$. This is caused by entrainment of the ambient plasma by the distorted magnetic field, as

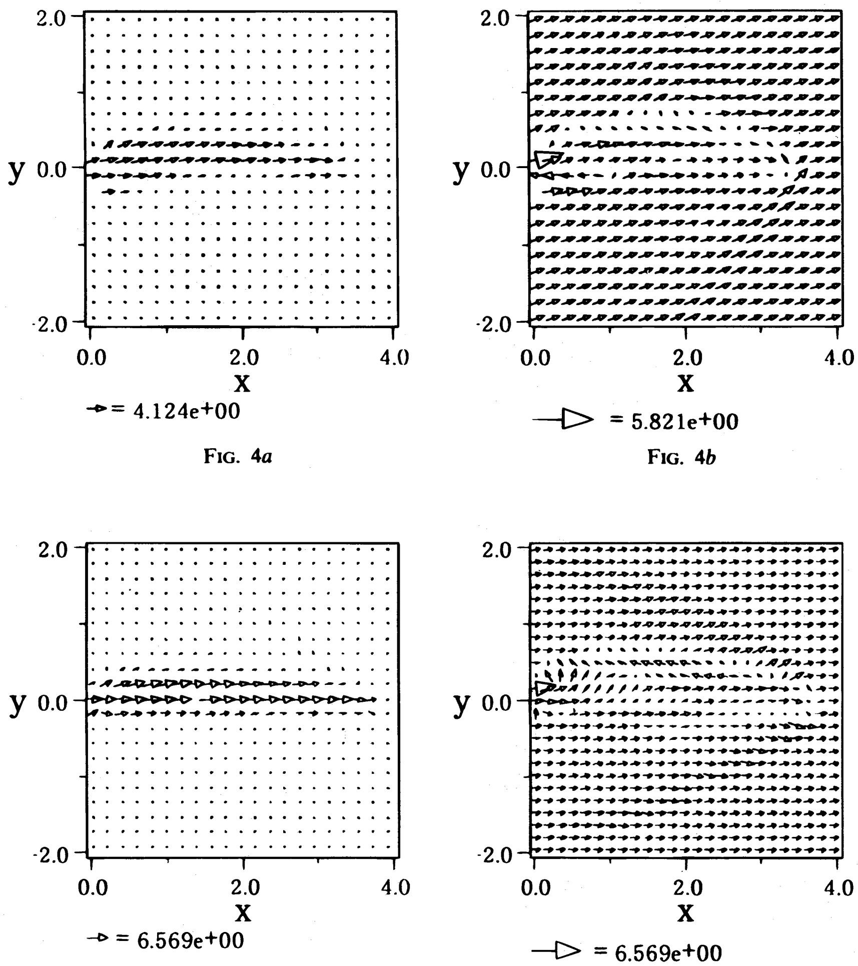

FIG. 4*a* FIG. 4*b* FIG. 4*c* FIG. 4*d*

FIG. 4.—Comparison of velocity (*a*, *c*) and magnetic field (*b*, *d*) for cases F and G. (*a*, *b*), Case F ($\theta = 15°$, $v_0 = 4v_A$) at $t = 1.74\tau_A$. (*c*, *d*) Case G ($\theta = 15°$, $v_0 = 7v_A$) at $t = 1.00\tau_A$.

TABLE 1

THE BENDING SCALE OF THE JET IN THE OBLIQUE MAGNETIC FIELD

Case (1)	v_0 (2)	θ (3)	R/a (4)	R_M/a (5)
A......	2	45°	4.55	6.30
B......	2.5	45	6.95	9.80
C......	3	45	10.1	14.2
D......	4	45	>15.0	25.2
E......	7	45	>17.5	50.5
F......	4	15	⩾20.0	77.0
G......	7	15	⩾20.0	154

TABLE 2

THE SCATTERING ANGLE OF THE JET BY THE OBLIQUE MAGNETIC FIELD

Case (1)	$\bar{v}_x$ (2)	$\bar{y}_y$ (3)	$\bar{v}_y/\bar{v}_x$ (4)	L (5)	$\tan \Delta\theta_M$ (6)
A......	0.702	0.636	0.906	1.42	0.282
B......	0.827	0.663	0.802	1.42	0.181
C......	1.14	0.198	0.174	2.07	0.183
D......	1.90	0.177	0.093	2.68	0.133
E......	...	...	...	3.63	0.059
F......	...	...	...	3.52	0.044
G......	...	...	...	3.72	0.015

TABLE 3

COMPRESSIBILITY AT THE JET HEAD OF ALL CASES

Case (1)	v_0 (2)	θ (3)	χ (4)	k (5)	ξ (6)	k_M (7)	ξ_M (8)
A......	2	45°	0.605	0.824	2.47	0.808	1.67
B......	2.5	45	0.725	0.729	2.85	0.516	2.60
C......	3	45	0.678	0.569	3.61	0.435	3.75
D......	4	45	0.640	0.478	4.67	0.354	6.67
E......	7	45	0.452	0.403	12.4	0.284	20.4
F......	4	15	0.532	0.281	5.26	0.354	6.67
G......	7	15	0.404	0.272	15.4	0.284	20.4

TABLE 4

THE DECELERATION EFFECT OF THE SPEED OF THE JET HEAD

Case (1)	v_0 (2)	θ (3)	v_h (4)	v_h^M (5)
A......	2	45°	0.702	0.437
B......	2.5	45	0.827	0.920
C......	3	45	1.14	1.42
D......	4	45	1.90	1.94
E......	7	45	3.60	3.36
F......	4	15	1.95	1.99
G......	7	15	3.72	3.48

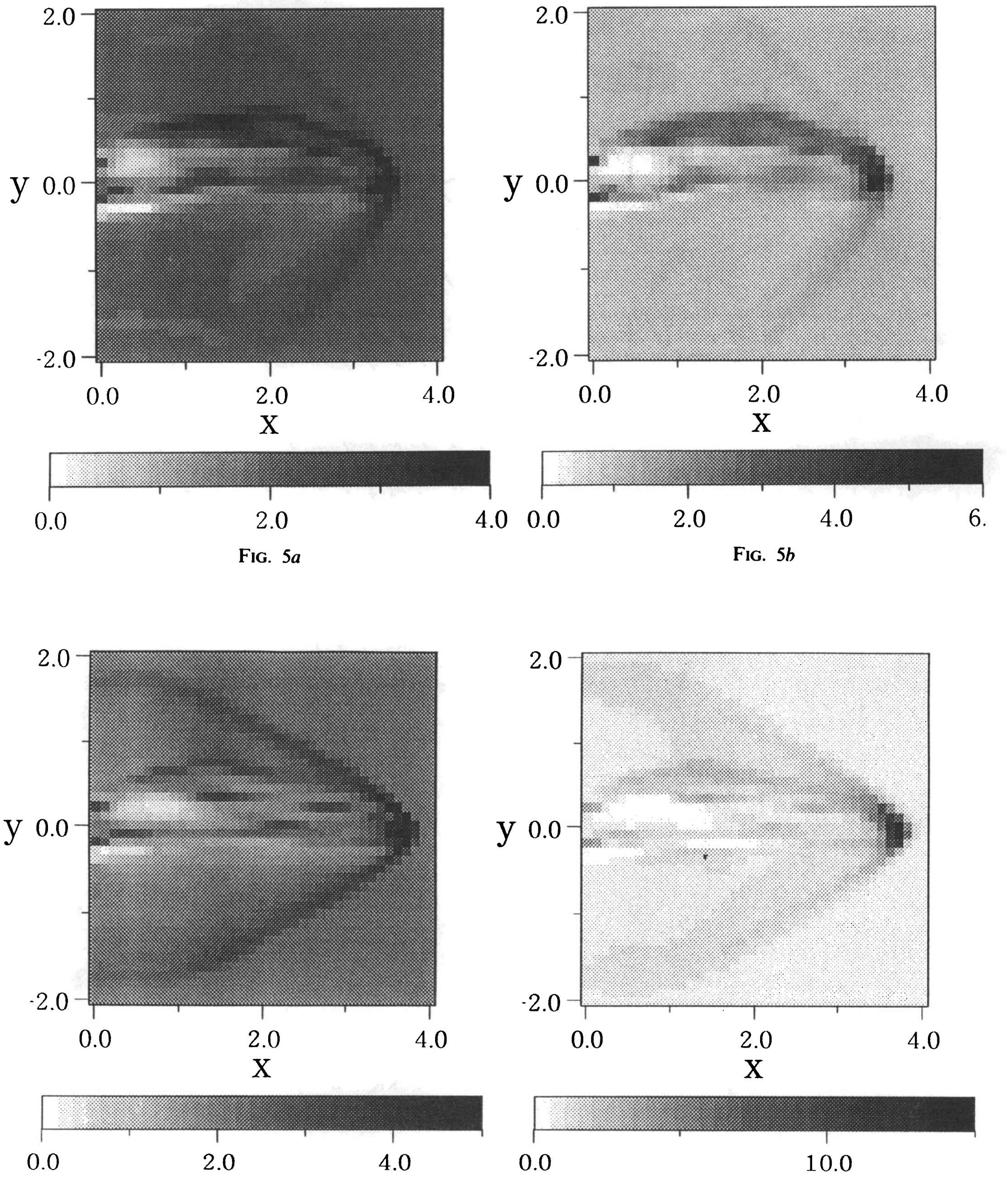

FIG. 5*a* FIG. 5*b*

FIG. 5*c* FIG. 5*d*

FIG. 5.—Comparison of density (*a*, *c*) and pressure (*b*, *d*) profiles for cases F and G. (*a*, *b*) Case F ($\theta = 15°$, $v_0 = 4v_A$) at $t = 1.74\tau_A$. (*c*, *d*), Case G ($\theta = 15°$, $v_0 = 7v_A$) at $t = 1.00\tau_A$.

described in the previous subsection. This effect can also be seen in the pressure plot (Fig. 8*c*). In this case, the density compression ratio $\chi \equiv \rho_a/\rho_b$ is 0.640, where subscripts "*a*" and "*b*" denote the ambient value and the highest value around the bow shock. The perpendicular component of the magnetic field is also compressed. The magnetic field compression ratio $k \equiv B_{ya}/B_{yb}$ is 0.478. The density compression ratio is larger than that of the magnetic field because the plasma can escape along the magnetic field lines. The pressure compression ratio $\xi \equiv p_b/p_a$ is 4.67. Note that the definitions of χ and ξ are the inverse of those defined by Königl (1980). Numerical experiments show that the pressure compression ratio is much stronger than that of density and magnetic field. The compressibility of all cases is summarized in Table 3 (cols. [4]–[6]).

The speeds of the jet heads were checked with the same jet velocity ($v_0 = 7v_A$) but using the different angles. Figure 9 shows the difference between the position of the jet head of cases E and G jets as a function of time. Until $t = 0.4\tau_A$, these jet heads locate at the almost same position. After $t = 0.6\tau_A$, we can see clearly that the low-angle jet (case G) is faster than the large-angle case jet (case E) with the velocity difference $\Delta v_h \sim 0.12v_A$. This shows the deceleration effect by the oblique magnetic field. The speeds of the jet heads are summarized in Table 4 (col. [4]).

4. ANALYTICAL MODELS

We have developed a simple analytical model to compare with the results of the numerical experiments, as described in the previous section. First we mention the existence of

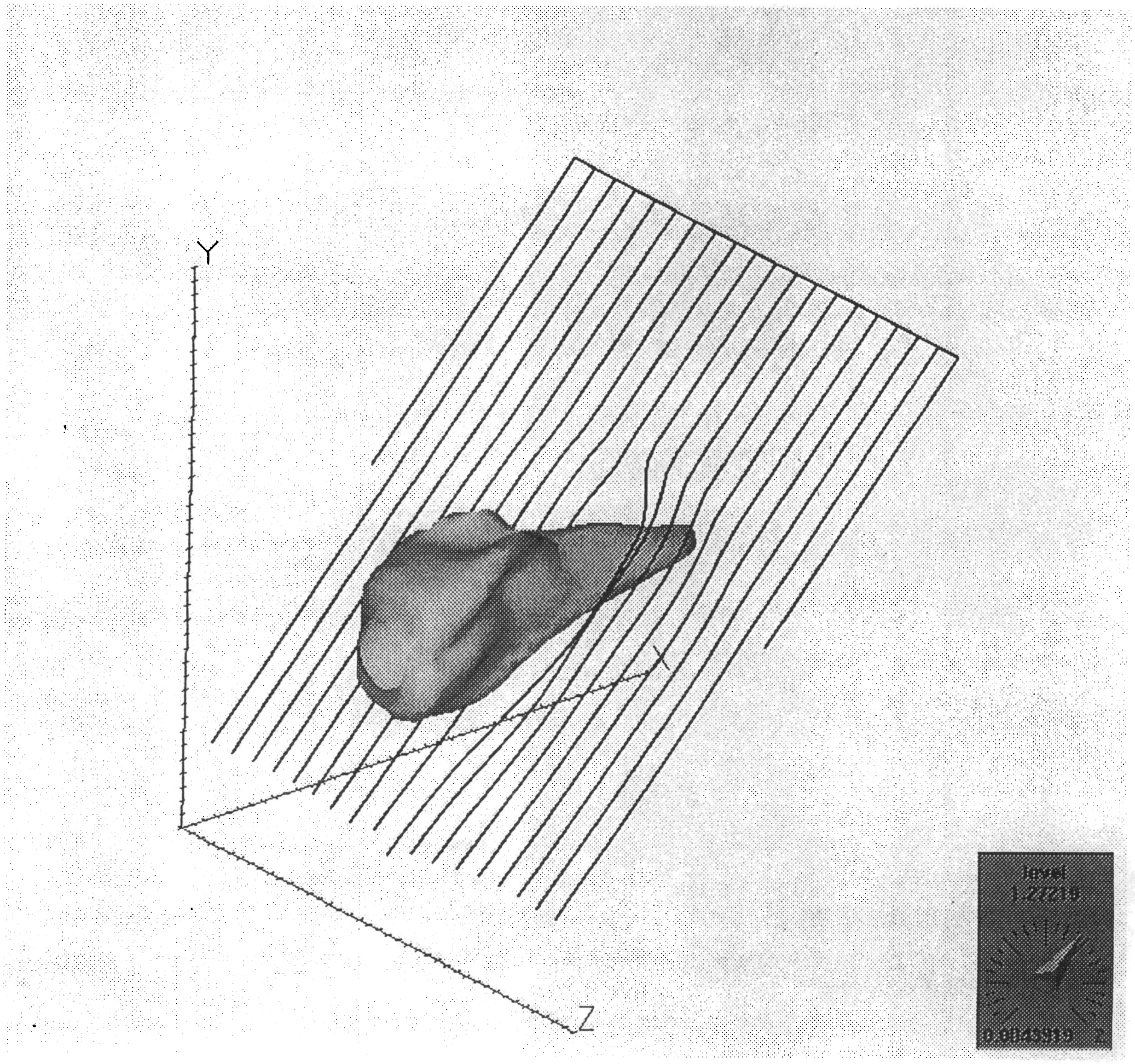

FIG. 6.—Three-dimensional structure of the jet in case E at $t = 1.24\tau_A$. The magnetic field is indicated by the field lines. The gray shade shows the velocity isosurface of $v_x = 1.74v_A$ which indicates the shape of the jet. The jet pushes the magnetic field aside as it propagates.

critical velocity $v_c \equiv [(2/\theta)\sin(\theta/2)/\eta]^{1/2}v_A \simeq v_A/\eta^{1/2}$ concerning the contribution of the magnetic tension. When $v_j \leq v_c$, the jet is bent very quickly by the magnetic tension. Case A ($v_0 = 2v_A$, $\theta = 45°$) corresponds to the case. In fact, the jet of case A is bent very quickly by the oblique magnetic field. On the other hand, when $v_j > v_c$, the jet propagates in a much more straight way than in the above case. We concentrate on the case with the condition $v_j > v_c$ because the extragalactic jet is expected to satisfy this condition. In this case, the bending scale of the jet by the ambient oblique magnetic field is estimated by a simple model (see Appendix) as

$$R_M = \frac{\pi}{2} a\eta M_A^2 \frac{1}{\sin 2\theta} , \qquad (14)$$

where $\eta \equiv \rho_j/\rho_a$ is the ratio between the density of the jet and the ambient plasma. Here we neglect the magnetic tension. Therefore, this expression gives the upper limit of the bending scale. However, as discussed in the Appendix, the bending scale is half the estimation at the shortest because the averaged value of magnetic pressure is comparable to that of magnetic tension. In the limit $\theta \to 0$, R_M becomes infinity as expected, which means no bending. In the limit $\theta \to \pi/2$, R_M also becomes infinity. This is plausible because infinite momentum is injected into the local area of ambient gas to push the perpendicular magnetic field. This expression is substantially in agreement with the numerical experiment, as shown in Table 1 (cols. [4] and [5]). It follows from this expression that jets with high velocity propagate further and more nearly straight, which agrees with the numerical result. It indicates also that the magnetic field with $\theta = 45°$ bends the jet most quickly. In fact, in the $\theta = 15°$ cases, we cannot observe the bending in our numerical experiment. For cases D, E, F, and G, the expected bending scales are larger than $50a$, which corresponds to no jet bending in the numerical experiment.

A simple model with an assumption of small scattering angle (see Appendix) yields the expression of the scattering angle of the jet by the oblique magnetic field as

$$\tan \Delta\theta_M = \frac{1}{2\pi} \frac{L}{a} \frac{1}{\eta M_A^2} \sin^2 2\theta , \qquad (15)$$

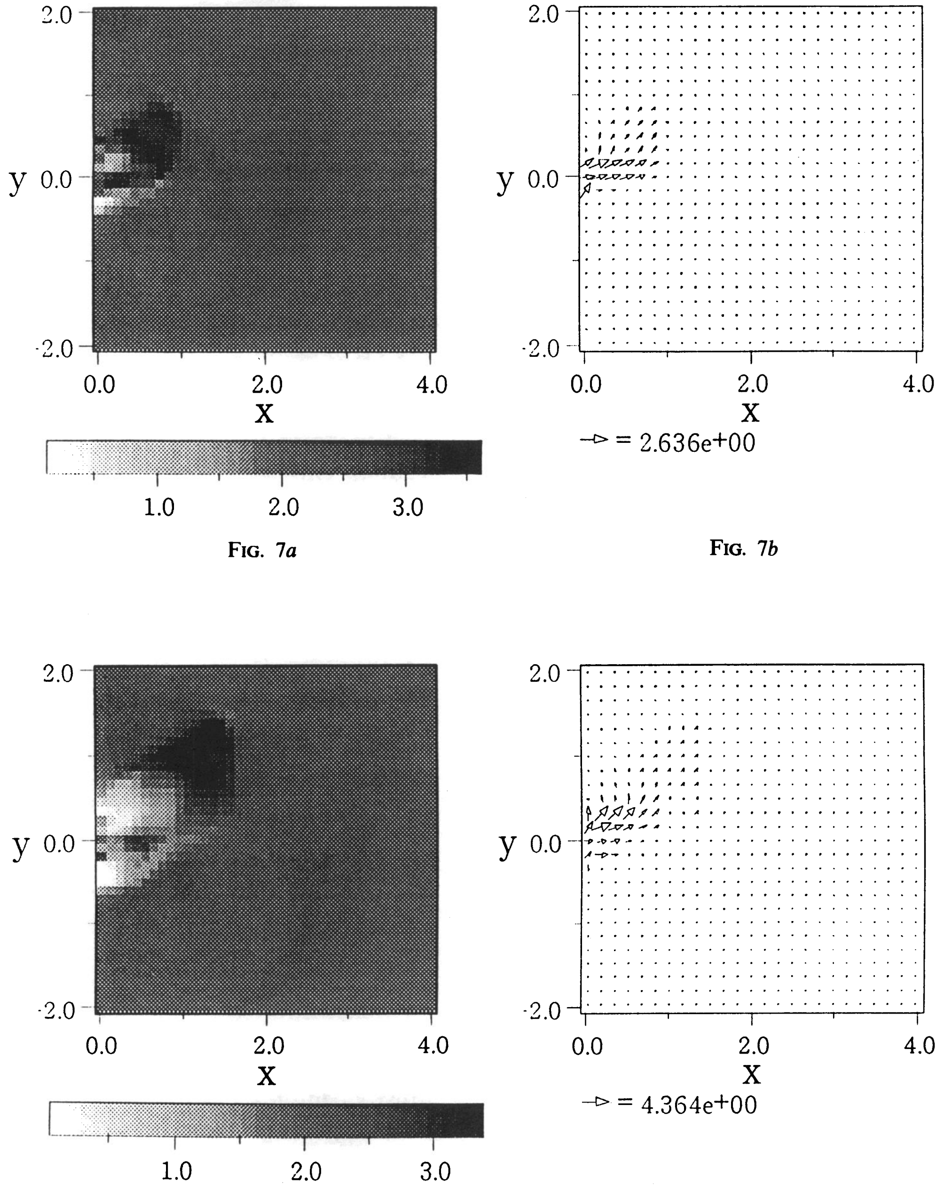

FIG. 7*a*

FIG. 7*b*

FIG. 7*c*

FIG. 7*d*

FIG. 7.—Density gray-scale plots (*a*, *c*) and velocity vector plots (*b*, *d*) of case A at $t = 1.00\tau_A$ (*a*, *b*) and $t = 1.87\tau_A$ (*c*, *d*)

where L is the traveling distance of the jet. Here we use a small scattering angle approximation. In the limit $\theta \to 0$ and $\theta \to \pi/2$, no bending is in agreement with the bending scale R_M limits given above. The $\theta = \pi/4$ oblique magnetic field scatters the jet most quickly. This expression agrees with the scattering angles found by the numerical experiments as shown in Table 2 (cols. [4], [6]). We found a good agreement in cases C and D. The difference in cases A and B is because the scattering angle is not small, as was assumed in equation (15). Unfortunately, in cases E, F, and G, the scattering angle could not be measured because it is less than 0.06 rad. Comparison between cases D and F clearly shows the dependence of the jet–magnetic field angle on the scattering angle. This expression yields the averaged scattering angle by an isotropic turbulent magnetic field as

$$\langle \Delta\theta \rangle = \frac{4}{15\pi} \frac{L}{a} \frac{1}{\eta M_A^2} . \quad (16)$$

In order to compare the observed compression of the plasma and perpendicular component of the ambient magnetic field at the jet head, we used a Rankine-Hugoniot relation at the front of the bow shock. The one-dimensional compression caused by passing through the sound shock is

$$k_M = \frac{1}{4} + \frac{3}{4} \left(\frac{v_s}{v_h} \right)^2 . \quad (17)$$

Here the sound speed v_s becomes the Alfvén speed when equipartition is assumed. In the one-dimensional model, the compression ratio of plasma density χ is the same as the density ratio k because of the frozen-in condition. The values calculated by this equation are shown in Table 3 (col. [7]). Here we use a simple expression of jet head speed without magnetic field. These calculated values k_M are in rough agreement with the numerical experiment results χ and k (Table 3, cols. [4]–[5]). In the numerical experiments, the density compression χ is larger than that of magnetic

1996ApJ...464..724K

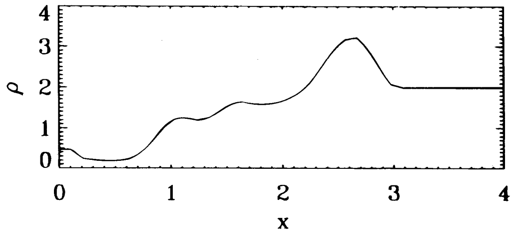

FIG. 8*a*

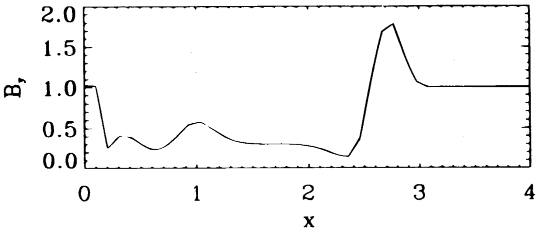

FIG. 8*b*

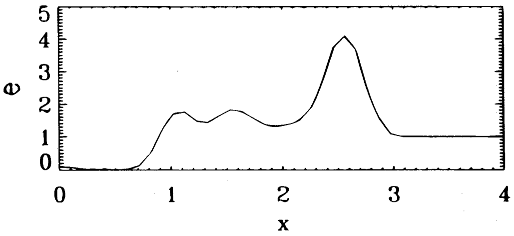

FIG. 8*c*

FIG. 8.—(*a*) Mass density (*b*) *y*-component of magnetic field, and (*c*) pressure for case D at the *x*-axis, which is almost the jet axis ($y = 0.20$, $z = 0.00$). The density, magnetic field, and pressure are compressed around the bow shock.

field k except for case A because the plasma can escape along the magnetic field lines. This effect is neglected in the simple one-dimensional model. The mumerical result shows that the density ratio k in case E ($v_0 = 4v_A$, $\theta = 15°$) is noticeably less than that of case D ($v_0 = 4v_A$, $\theta = 45°$). We can find the same effect in cases E ($v_0 = 7v_A$, $\theta = 45°$) and G ($v_0 = 7v_A$, $\theta = 15°$). This effect can be understood by noting that the magnetic pressure becomes important in the $\theta = 45°$ cases. Expression (17) asserts that χ and k must be larger than 1/4. We can confirm this restriction in Table 3 in the numerical results. The compressibility of the pressure at the jet head is determined by the balance between the ram pressure of the jet head $\rho_j(v_j - v_h)^2$ and the high pressure p_b as

$$\xi_M = \gamma\eta\left(\frac{v_s}{v_h}\right)^2 . \qquad (18)$$

The calculated values are shown in Table 3 (col. [8]). These values ξ_M are in good agreement with the results of numerical experiments. This expression indicates that the pressure at the jet head increases rapidly as the jet velocity increases. In fact, the numerical experiments of high-speed jet cases E and G show the extremely high compressibility at the jet head as shown in Table 3 (col. [6]).

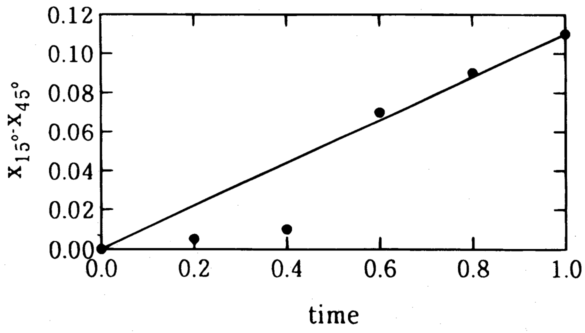

FIG. 9.—The difference between the position of the bow shock for case E and G jets as a function of time. We found the deceleration velocity of the jet by the oblique magnetic field from $t = 0.6\tau_A$ to $t = 1.0\tau_A$. Solid line indicates the average velocity difference between them.

The numerical experiments show the deceleration of the head speed by the oblique magnetic field (see the previous section). This effect is explained by the balance of ram pressure and magnetic pressure at the working surface. A simple one-dimensional model (see Appendix) yields

$$v_h^M = \frac{\sqrt{\eta'}}{1 + \sqrt{\eta'}}\, v_0 D , \qquad (19)$$

where

$$D = \frac{(1 - \sin^2\theta/\eta' k^2 M_A^2)(1 + \sqrt{\eta'})}{\sqrt{\eta'} + \sqrt{1 + (1 - 1/\eta')\sin^2\theta/k^2 M_A^2}} . \qquad (20)$$

This expression asserts that the speed of the jet must $M_A \geq \sin\theta\eta'^{-1/2}k^{-1}$ to propagate across the oblique magnetic field. In the limit $\theta \to 0$, v_h reduces to the well-known expression without magnetic field (Norman & Winkler 1985; Kochanek & Hawley 1990; Begelman & Cioffi 1989; Wiita, Rosen, & Norman 1990; Wiita & Norman 1992). This expression with $\eta' = 1$ agrees with the numerical experiment except for case A, as shown in Table 4 (cols. [4] and [5]). The predicted value for case A using equation (19) does not agree with the numerical result because the jet has already bent in a short distance. In a limit $\eta' k^2 M_A^2 \ll 1$ with $\eta' \leq 1$, equation (20) becomes

$$D \approx 1 - \frac{1 + \sqrt{\eta'}}{2}\,\frac{\sin^2\theta}{\eta' k^2 M_A^2} . \qquad (21)$$

5. DISCUSSION

We investigated the propagation of jets injected obliquely into ambient uniform magnetic fields using the three-dimensional MHD code ZEUS-3D and simple analytical models. The results are summarized as follows:

1. The oblique magnetic field bends the jet. We found that the morphology of the jet propagation depends on the jet velocity in the case of $\theta = 45°$. For the case with Mach number $M_A \leq 2$, the jet is bent very quickly by the oblique magnetic field because of $v_j \leq v_c$, where v_c is critical velocity for magnetic tension effect. For $2 < M_A < 4$, the jet seems to spread and split before bending. If $M_A \geq 4$, the jet propagates almost straight, but eventually it bends. In this case, magnetic tension is negligible. The bending scale and scattering angle of the jet propagation by the oblique magnetic field were investigated by the numerical experiment and simple models (eqs. [14]–[15]): when $M_A > 2$, magnetic tension is negligible. We found good agreement between the simple models and the numerical experiment for most cases. They show clearly that the jet with the high velocity propa-

gates further and without measurable bending. They also indicates that an oblique magnetic field at $\theta = 45°$ bends the jet with the shortest traveling distance compared with any other angles. Equation (16) yields the averaged scattering angle by the isotropic turbulent magnetic field.

2. The plasma density and the perpendicular component of magnetic field in front of the jet are compressed. The compressibility of the magnetic field and plasma density increases as the velocity of the jet increases. The compressibility is given by the Rankine-Hugoniot relation (eq. [17]) at the bow shock of the jet head. The plasma pressure at the jet head also increases as the jet velocity increases. The compressed pressure is given assuming balance between the incident ram pressure of the jet and the pressure at the head as described by equation (18). They show that the pressure at the jet head is proportional to the square of the jet velocity, while the density and perpendicular component of the magnetic field at the head must be larger than 1/4.

3. The oblique magnetic field decelerates the speed of the jet head. The simple model described by equation (19) agrees substantially with the results of the numerical experiment. This simple model shows dependence of the deceleration rate of the jet on the angle between the initial jet velocity and magnetic field.

Now we apply these results to explain the jets of BL Lacertae objects. Recent VLBI observations have revealed three kinds of impressive peculiarities of BL Lacertae objects within the unified scheme of AGNs. First, the magnetic field at the knot is perpendicular to the parsec-scale structure of BL Lacertae objects while parallel to nuclear jets in quasars. Second, the flow speeds of BL Lacertae objects are systematically less than those of quasars. The third peculiarity is a statistical remark; that is, for almost all BL Lacertae objects, one-sided jet structures at parsec and kiloparsec scales are strongly misaligned, while for some of quasars and extragalactic jet they are more nearly aligned.

Sol (1992b) and Sol & Vicente (1995) proposed the model of the jet injected into the oblique magnetic field to explain some of these pecularities. They considered the oblique coherent magnetic field tied with the accretion disk whose rotation axis is different from the jet axis. But the scale of the accretion disk is much smaller than 1 pc, which is the order of the VLBI resolution, so it is improbable that such a magnetic field held by the accretion disk has influence on the kilo-parsec scale structure of BL Lacertae objects. Jones et al. (1985) analyzed the magnetic field around BL Lacertae objects as a turbulent field. Therefore, the model of a jet injected into the turbulent ambient magnetic field is more plausible for BL Lacertae objects. These peculiarities and the lack of the emission line of BL Lacertae objects may be explained by an assumption that the extragalactic magnetic field of 1″ scale around BL Lacertae objects is turbulent, while that of quasars is coherent.

Recently, X-ray spectrum analysis has estimated the magnetic field strength $B_0 \sim 20$ mG (Tashiro et al. 1995; Sambruna et al. 1995). This observational value is expected for the compressed magnetic field at the jet head. The compression rate is greater than 1/4. Therefore, the ambient magnetic field strength is greater than $B_a \sim 5$ mG. We also determine $\eta \sim 0.01$ from the observational shape of jet (Norman 1990). A recent VLBI observation has determined the radius of the cross section of the jet $a \sim 0.5$ pc (Appl et al. 1995). Jones (1985) determined the characteristic length of the turbulent magnetic field around BL Lacertae objects $l_B \sim 0.2a$. Many authors (Begelman, Blandford, & Rees 1984; Gabuzda, Wardle, & Roberts 1989*b*; Hughes, Aller, & Aller 1989; Mutel 1989; Mutel et al. 1990) have concluded that the jet is relativistic, $v_h \sim c$, $v_j \sim c$, where c is light velocity. In this case, the Alfvén Mach number is $M_A \sim 30$. Here we neglect the relativistic effect to evaluate the rough but essential estimation of the BL Lacertae objects. The relativistic effect is considered in our following work. We choose other parameters based on the work by Sol & Vicente (1995) as follows: $n_a \sim 10^6$ m^{-3} and $\eta' \sim \eta \sim 0.01$.

We are aware that our nonrelativistic MHD simulations cannot be applied to explain observations with BL Lac objects directly. Furthermore, BL Lac objects consist of electron-positron plasmas; therefore, an electromagnetic, relativistic particle code (Zhao et al. 1994) would be necessary to include kinetic effects which are essential in electron-positron plasmas. However, the main features of our simulations would apply in observations with BL Lac objects. First we discuss the peculiarity of jet bending of BL Lacertae objects. Hardee (1987), Hardee et al. (1994), and Conway & Murphy (1993) proposed the model of Kelvin-Helmholtz instability to explain the misalignment of nuclear jets of AGNs. Other mechanisms of the bending were proposed, e.g., a precessing of a binary engine (Begelman et al. 1980) and deflection of the jet in a dense ambient medium (Ludke 1994). Bending of the jet by interaction with an ambient magnetic field is discussed. The bending scale of the jet by the turbulent magnetic field is estimated as follows. First we assume that the ambient medium is uniform and injection angle $\theta = 45°$ to evaluate the shortest length. The bending scale is then estimated to be $R_M = 28a$ by equation (14). But according to Jones et al. (1985), the ambient magnetic field is turbulent, with the characteristic length of $0.2a$. This length is much less than that of bending. Hence, the influence of the turbulent magnetic field is regarded as the small-angle scattering of the jet by one coherent piece of the turbulent magnetic field. Many small-angle scatterings may produce large bending of the jet. This mechanism is regarded as a random walk process. We can estimate the final scattering angle Θ as

$$\Theta = \langle \Delta\theta \rangle \sqrt{\frac{L}{l_B}} ,$$

where $L \sim 1$ kpc is the traveling distance of the jet and $l_B \sim 0.1$ pc is the characteristic length of the turbulent magnetic field. This yields $\Theta \sim 0.2$(rad) with equation (16), which shows that the turbulent ambient magnetic field can bend the jet of the BL Lacertae object. This bending mechanism by the ambient turbulent magnetic field becomes important for the jets of BL Lacertae objects. This additional bending mechanism explains the third peculiarity of BL Lacertae objects.

Furthermore, our MHD numerical experiment confirms that the plasma and the perpendicular component of the ambient oblique magnetic field are compressed at the head of the jet, as mentioned in the above item (2). The jets of BL Lacertae objects go through a substantially oblique magnetic field because of the turbulent magnetic field, while those of quasars are parallel to the magnetic field in milliarcsecond scale. We calculate the enhancement of the synchrotron radiation to estimate the intensification of the polarized radiation. A simple model yields the emissivity as $\epsilon = 4\sigma_{\rm T} pB^2/(2\mu m_e c)$, where $\sigma_{\rm T}$ is the Thomson cross section and m_e is mass of the electron. The enhancement ratio of the polarized emissivity ϵ at the jet head to that of the bulk of jet and ambient plasma is 6000 for the oblique jet to the ambient magnetic field. This enhanced synchrotron radiation may hide the emission lines in BL Lacertae objects. In fact, recently the emission lines of BL Lacertae objects have become stronger compared to synchrotron radiation and observed more clearly (Vermeulen et al. 1995). The enhancement of the synchrotron radiation may make the perpendicular component of the turbulent magnetic field around BL Lacertae objects dominant at the jet head which is observed as the knot by VLBI, while no enhancement of the perpendicular component of the coherent around quasar is expected. The assumption explains both the lack of an emission line and the first peculiarity of BL Lacertae objects.

The model of a jet injected to the oblique magnetic field also explains the second peculiarity. Our numerical experiment confirms the deceleration of the jet head by the oblique magnetic field. We estimate that the deceleration rate $D = 0.28$ where $\theta = 45°$ for average and $k = 1/4$. This means that the oblique magnetic field decelerates the jet head to one-fourth of the speed without the ambient magnetic field (see eq. [19]). On the other hand, the deceleration of the jet head speed of the quasar by the ambient magnetic field is not expected because of its parallel coherent magnetic field.

The model of the jet injected into the ambient random magnetic field may explain the three peculiarities and the lack of an emission line in BL Lacertae objects.

In this paper, we have assumed a nonrelativistic jet, which is clearly inappropriate for many extragalactic radio jets. We will consider the bending of relativistic jets in a forthcoming paper.

We thank Mickel L. Norman and Robert Fiedler for useful discussions and hospitality during our visit at National Center for Supercomputing Applications. K.-I. N. thanks Hélène Sol and Lourdes Vicente for their important discussion. S. K. thanks Mika Inda-Koide for her important comments. This work is supported by the U.S.-Japan cooperative science program JSPS and NSF (INT-9217650). S. K. appreciates helpful discussion at the Workshop on Energy Transport in Radio Galaxies and Quasars in Alabama organized by Philip E. Hardee and Alexander Rosen. He thanks Jagbir S. Hooda for his kind discussion. K.-I. N. is supported by the National Science Foundation under Grant nos. ATM-9119814 and ATM-9121116.

APPENDIX

We derive a simple estimation of the bending length R_M and the scattering angle of the jet by the oblique magnetic field $\Delta\theta_M$. Both the gradient in magnetic pressure and the tension of the bent magnetic field lines have the tendency to stop and bend the jet. Here we neglect the magnetic tension. This estimation yields the upper limit of the bending scale. The force density of the magnetic pressure and tension are estimated by $f_p = |\nabla B^2/2| \sim B^2/2L$ and $f_t = |(\boldsymbol{B} \cdot \nabla)\boldsymbol{B}| \sim B^2/R$, respectively. Here R is the radius of curvature of the magnetic field and L is the characteristic length of magnetic pressure gradient by the jet. When $R \sim 2L$, we obtain $f_p \sim f_t$. In fact, we found that the averaged value of magnetic pressure is comparable to that of magnetic tension beside the jet in our simulation results. Therefore, the bending scale is half the estimation at the shortest (see following equations). Figure 10*a* shows the initial jet propagating through the oblique magnetic field (*solid line*) and eventually the bent jet (*dotted line*). We separate the initial velocity of the jet into the parallel and perpendicular components with respect to the ambient magnetic field. We consider the coordinate system O'-$x'y'z'$, whose velocity is the same as the parallel velocity of the jet. In this new coordinate system, the jet is injected perpendicularly to the ambient magnetic field, with the velocity $v_0 \sin\theta$ (Fig. 10*b*). The orifice of the jet moves along the magnetic field with the velocity $v_0 \cos\theta$ as well as the ambient medium. Therefore, the velocity of the jet is not parallel to the axis of the jet. The kinetic energy per unit length is $\pi a^2 \rho_j (v_0 \sin\theta)^2/2$. The magnetic field on the jet boundary is estimated as B_a. The jet also contains magnetic field $B_a \cos\theta$. The force per unit length from the ambient magnetic field to the jet is $aB_a^2 \sin^2\theta$. We can define a geometrical factor $S \equiv \sin^2\theta$. The jet stops at a distance R' on the new coordinate system, which satisfies

$$\frac{1}{2}\pi a^2 \rho_j (v_0 \sin\theta)^2 = aB_a^2 S R' \cos\theta .$$

When the jet stops on the new coordinate system, it propagates along the magnetic field, i.e., it already bends on the original coordinate system. The distance R_M of the bending in the original coordinate system is estimated to be

$$R_M = \frac{R'}{\sin\theta} = \pi a \eta M_{\rm A}^2 \frac{1}{\sin(2\theta)} .$$

The force perpendicular to the jet $aB_a^2 S/t$ accelerates the jet perpendicular to the jet with the velocity $v_\perp$ in the original coordinates when the jet goes almost straight. The perpendicular velocity is estimated by the equation

$$\pi a^2 \rho_j v_0 = aB_a^2 St ,$$

where traveling time t is given by the traveling distance L and the jet head velocity v_h as $t = L/v_h$. The perpendicular velocity $v_\perp$ is given by

$$v_\perp = \frac{1}{\pi a}\frac{1}{\eta} v_{\rm A}^2 S \frac{L}{v_h} .$$

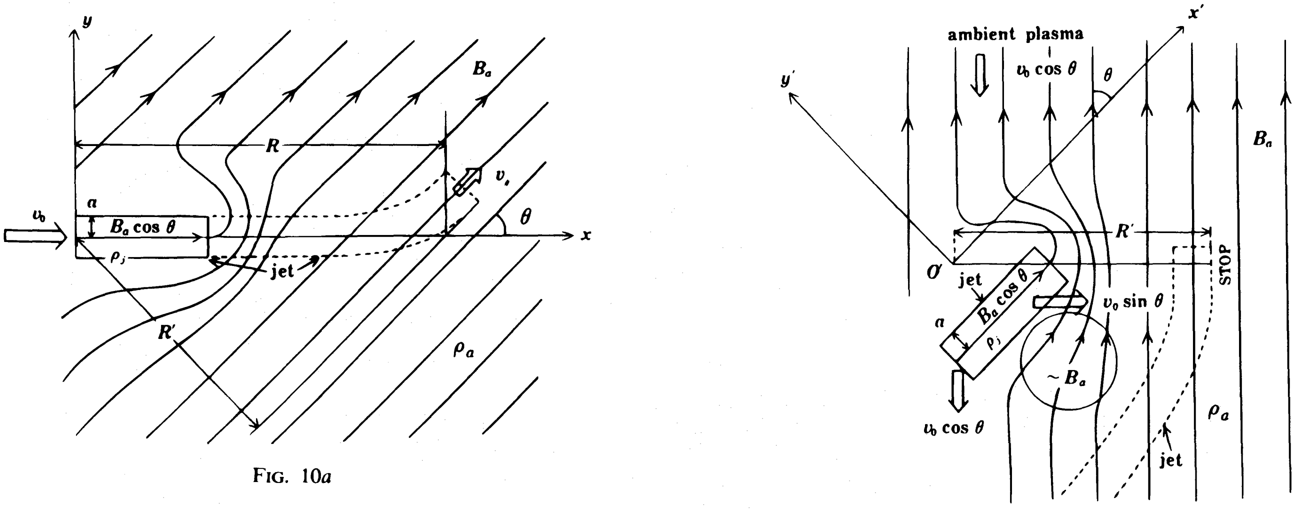

FIG. 10*a*

FIG. 10*b*

FIG. 10.—The schematic picture of the jet propagation through the oblique magnetic field in the different coordinates. (*a*) The jet is propagating across the oblique magnetic field in the original coordinates $O - xyz$, where the ambient plasma is rest. (*b*) The oblique jet is injected perpendicularly into the ambient magnetic field in the new coordinates $O' - x'y'z'$. The orifice of the jet moves downward, the same as the ambient plasma.

When we use $v_h = (\eta')^{1/2} v_0 / [1 + (\eta')^{1/2}]$, we obtain the scattering angle by the oblique magnetic field:

$$\tan \Delta\theta = \frac{v_\perp}{v_0} = \frac{L}{2\pi\eta a M_A^2} \sin^2 2\theta \, .$$

We derive the expression (19) of the deceleration of the jet by the oblique magnetic field. In the coordinate frame at rest with respect to the jet head, the balance between the ram pressure and ambient magnetic field is given by

$$\rho(v_0 - v_h)^2 S_j = S_h \left[\rho_a v_h^2 + \frac{B_a^2}{\mu} - \frac{(B_a^2 \cos\theta)^2}{\mu} \right] , \tag{22}$$

where we approximate the magnetic field at the front of the jet by the initial magnetic field. Here we neglect the contribution of pressure. This assumption is valid when the pressure inside the jet is the same as that of the ambient plasma. We can solve this equation easily as

$$v_h = \frac{-\eta' v_0 \pm \sqrt{(\eta' v_0)^2 - (1 - \eta')(v_0^2 \eta \sin^2\theta - \eta' v_0^2)}}{1 - \eta'} \, . \tag{23}$$

We have to take the plus sign on the numerator of the right-hand side because of the direction of the jet. We replace M_A with kM_A considering the compression effect at the side of the jet. After some algebra, we find equations (19).

REFERENCES

Appl, S., Sol, H., & Vicente, L. 1996, A&A, in press
Begelman, M. C., Blandford, R. D., & Rees, M. J. 1980, Nature, 287, 307
———. 1984, Rev. Mod. Phys., 56, 225
Begelman, M. C., & Cioffi, D. F. 1989, ApJ, 345, L21
Conway, J. E., & Davis, R. 1994, A&A, 284, 724
Conway, J. E., & Murphy, D. W. 1993, ApJ, 411, 89
Fejes, R., Porcas, R. W., & Akujor, C. E. 1992, A&A, 257, 459
Gabuzda, D. C. 1992, in Extragalactic Radio Sources From Beam to Jets, ed. J. Roland, H. Sol, & G. Relletein (Cambridge: Cambridge Univ. Press), 145
Gabuzda, D. C., Cawthorne, T. V., Roberts, D. H., & Wardle, J. F. C. 1989a, ApJ, 347, 701
Gabuzda, D. C., Mullen, C. M., Cawthorne, T. V., Wardle, J. F. C., & Roberts, D. C. 1994, ApJ, 435, 140
Gabuzda, D. C., Wardle, J. F. C., & Roberts, D. H. 1989b, ApJ, 336, L59
Hardee, P. E. 1987, ApJ, 318, 607
Hardee, P. E., & Clarke, D. C. 1992, ApJ, 400, L9
Hardee, P. E., Michael, A. C., & Clarke, D. A. 1994, ApJ, 424, 126
Hardee, P. E., White, R. E., III, Norman, M. L., Cooper, M. A., & Clarke, D. A. 1992, ApJ, 387, 460
Hughes, P. A., Aller, H. D., & Aller, M. F. 1989, ApJ, 341, 68
Hummel, C., Muxlow, T., Krichbaum, T., Quirrenbach, A., Schalinski, C., Witzed, A., & Johnston, K. J. 1992, A&A, 262, 295
Jones, J. W., Rudrick, L., Aller, H. D., Aller, M. F., Hodge, P. G., & Fiedler, R. L. 1985, ApJ, 290, 627
Kochanek, C. S., & Hawley, J. F. 1990, ApJ, 350, 561
Königl, A. 1980, Phys. of Fluids, 23, 1083
Ludke, E. 1994, Ap. Space Sci., 216, 369
Mutel, R. L. 1989, in Proc. Parsec Scale Radio Jet Workshop, Socorro, NM, ed. J. A. Zensus & K. I. Kellerman (Green Bank: NRAO), 191
Mutel, R. L., Phillips, R. B., Su, B., & Bucciferro, R. R. 1990, ApJ, 352, 81
Norman, M. L. 1990, in Ann. NY Acad. Sci., 617, Nonlinear Astrophysical Fluid Dynamics, ed. J. R. Buchler & S. T. Gottesman (New York: NY Acad. Sci.), 217
Norman, M. L., & Winkler, K.-H. A. 1985, Los Alamos Science, 12, 38
Sambruna, R. M., Urry, C. M., Ghisellini, G., & Maraschi, L. 1995, ApJ, 449, 567
Sol, H. 1992a, in Extragalactic Radio Sources from Beams to Jets, ed. J. Roland, H. Sol, & G. Pelletier (Cambridge: Cambridge Univ. Press), 264
———. 1992b, C. R. Acad. Sci. Paris, 315, 1481
Sol, H., Appl, S., & Vicente, L. 1995, in IAU Symp. 175, Extragalactic Radio Sources, in press
Sol, H., & Vicente, L. 1994, in IAU Symp. 159, Multi-Wavelength Continuum Emission of AGN, ed. T. J.-L. Courvoisier & A. Blecka (Dordrecht: Kluwer), 473
———. 1995, A&A, submitted
Stone, J. M., & Norman, M. L. 1992a, ApJS, 80, 753
———. 1992b, ApJS, 80, 791
Tashiro, M., Makishima, K., Ohashi, T., Inda-Koide, M., Yamashita, A., Mihara, T., & Kohmura, Y. 1995, PASJ, 47, 131
Vermeulen, R. C., Ogle, P. M., Tran, H. D., Browne, I. W. A., Cohen, M. H., Readhead, A. C. S., & Taylor, G. B. 1995, ApJ, 452, L5
Wiita, P. J., & Norman, M. L. 1992, ApJ, 385, 478
Wiita, P. J., Rosen, A., & Norman, M. L. 1990, ApJ, 350, 545
Zhao, J.-H., Burns, J. O., Norman, M. L., & Sulkanen, M. E. 1992, ApJ, 387, 83
Zhao, J., Sakai, J.-I., Nishikawa, K.-I., & Neubert, T. 1994, Phys. Plasmas, 1, 4114